Fluorescence confocal scanning microscopy for pH mapping in a coaxial flow microreactor: application in the synthesis of superparamagnetic nanoparticles

Ali Abou Hassan, Jean-François Dufrêche, Olivier Sandre, Guillaume Mériguet, Olivier Bernard, Valérie Cabuil

HAL Id: hal-00428983
https://hal.science/hal-00428983

Submitted on 26 May 2019

Graphical and textural abstract

The utilization of fluorescence confocal laser scanning microscopy (CLSM) to quantify pH gradients is described and compared to the results of numerical simulations in a coaxial flow microreactor for applications in the synthesis of superparamagnetic iron oxide nanoparticles.
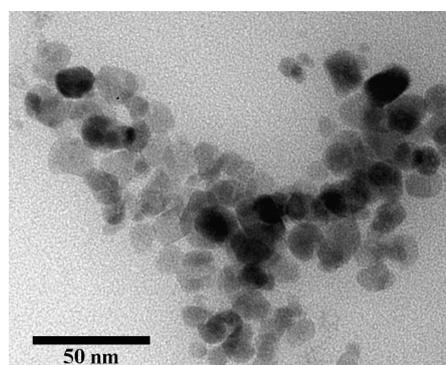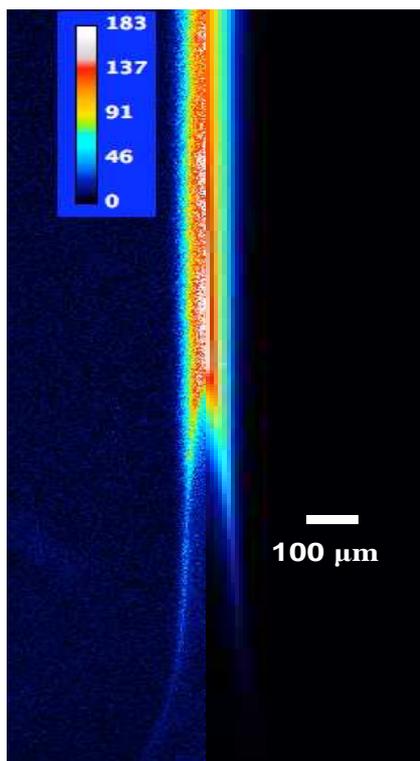
FULL PAPER

J. Phys. Chem. C 2009 **113** 18097-18105

Fluorescence confocal laser scanning microscopy for pH mapping in a coaxial flow microreactor: application in the synthesis of superparamagnetic nanoparticles

Ali Abou-Hassan,*[a] Jean-François Dufrêche,*[a] Olivier Sandre,[a] Guillaume Mériguet,[a] Olivier Bernard,[a] and Valérie Cabuil[a]

The application of fluorescence confocal laser scanning microscopy (CLSM) to quantify three dimensional pH gradients in a coaxial flow microreactor is described. The methodoloy consits in utilizing a micromolar concentration of the common dye fluorescein, which fluorescence in solution strongly increases above pH 6.2, in order to map the pH changes in the central jet stream where an acid-base reaction proceeds. The experimental fluorescence profiles determined by CLSM, have been comprared to models by solving the underlying mass transport equations using the finite element method. The fluorescence profiles were found to be highly sensitive to both the initial bulk solution pH and the applied volumetric rate ratio (α) of the outer stream to the inner stream. The simulated pH gradients have been compared for different α leading to an optimal value for the preparation of superparamagnetic nanoparticles.

1 Introduction

In the past decade, the synthesis of superparamagnetic iron oxide nanoparticles has been intensively developed for fundamental scientific interest and also for many technologies. Superparamagnetic iron oxides are used for magnetic storage media,[1] hyperthermia,[2] biosensing applications,[3] targeted drug delivery,[4] and as contrast agents in magnetic resonance imaging (MRI).[5] The properties of the finely devided magnetic materials closely depend on the size of the particles and their state of dispersion or aggregation. In the case of quantum dots where the monodispersity of diameters is crucial for the fluorecence properties, microfluidics has been proposed to control the conditions of synthesis more accurately than in the bulk.[6] Since then, microfluidic reactors have been designed to produce nanoparticles of a wide number of materials.[7] Among these, superparamagnetic iron oxide nanoparticles have been prepared for the first time by our group in a coaxial flow microreactor that achieves small diffusion distances and fast mixing times.[8] Later on, the setup was improved by separating a nucleation reactor and an aging channel in order to synthesize antiferromagnetic ferrihydrite nanolaths.[9] Microfluidic offers several advantages over batch reactors for controlling the synthesis and the growth of nanoparticles. For example, stationnary concentration or temperature gradients can be tuned during the synthesis of nanoparticles in order to improve their monodispersity.[10-12] We have focused our attention on building up pH gradients in a microfluidic mixer because pH is a parameter of uppermost importance during the synthesis of nanoparticles by coprecipitation reactions of precursor salts and it remains also a key parameter for their properties (e.g. charge) and their stability in the final colloidal solution. Based on some assumptions, this paper reports experimental and theoretical studies of pH gradients in the coaxial microreactor for nanoparticles synthesis.
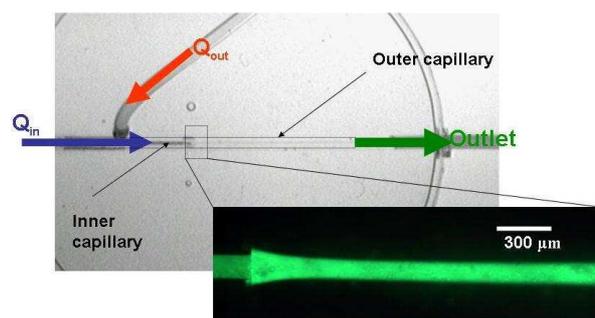

Fig. 1 Coaxial flow device studied in this paper. The inset shows an epifluorescence image of the flow from the inner capillary labelled with a fluorescent dye. The inner flow appears bright while non fluorescent buffer flows from the side channel.

Several methods probe concentration gradients locally by utilizing the optical properties of either generated or consumed species. These techniques include interferometry[13] and spectroscopic approaches such as Raman spectroscopy[14] and confocal resonance Raman microscopy.[15] Several other techniques based on light absorption rather than refractive index as spatially resolved absorbance electrochemistry[14] and micro X-rays absorption spectroscopy[16] have been used to provide informations on local scale concentration gradients. High-resolution nuclear magnetic resonance imaging and electrochemical techniques have recently proven particularly powerful for observing concentration gradients at both electrode surfaces and liquid/liquid interfaces.[17]

Optical imaging by fluorescence has found particular application in the vizualization of pH gradients. Compared to conventional fluorescence microscopy, confocal laser scanning microscopy (CLSM) reduces out of focus blur that

18097 | *J. Phys. Chem.* C 2009, **113**, No. 42

Abou-Hassan et al, author manuscript

would otherwise result from light being collected both above and below the focal plane of the objective. CLSM allows direct, noninvasive, serial optical sectioning of objects and profiling of multilayer structures.[18]

This paper attempts to address the pH gradients in the coaxial flows microreactor, which will be an important parameter in further experimentation for nanoparticles synthesis. The systems considered herein are the chemical reaction between the hydrochoric acid flowing in the inner focalised flow and the alkaline solution of tetamethylamonium hydroxide flowing in the outer flow. In our study, fluorescein is used as a probe to map the pH gradients. Experimental CLSM results are compared to numerical simulations of the spatial distribution of the fluorecein concentration and of pH in both the inner jet and the surrounding stream.
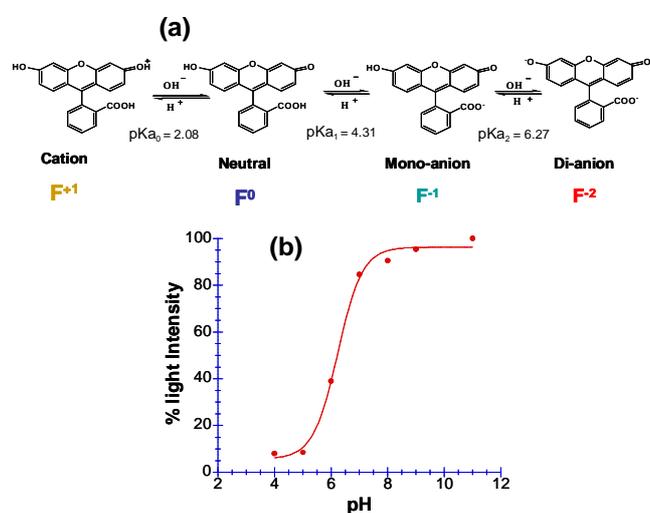
2 Experimental

2.1 Materials

Fig. 2 (a) Chemical structures of fluorescein based on different pH. Fluorescein is a cation at pH < 2.08, neutral at 2.08 < pH < 4.31, an anion at 4.31 < pH < 6.27, and a dianion at pH > 6.27. (b) Percentage light intensity relatively to the value at pH 11 as a function of pH for a solution of 6 μM disodium fluorescein.

Fluorescein is a well-known pH sensitive dye. Its molecular structure becomes progressively deprotonated when pH increases, as shown on Fig. 2. The only fluorescent species is the di-anion F^{-2} and in a much lower extend the mono-anion F^{-1}. As the pH rises in an aqueous solution, the fluorescence signal increases starting at pH~5 and saturating at a maximum value above pH~7. To verify the pH dependence of the signal, a stock solution of disodium fluorescein was prepared and diluted at 6 μM in different pH-buffered solutions. The solutions were perfused in both the inner and outer capillaries and the corresponding fluorence images were captured with the CLSM at the median plane of the channel (i. e. far from the walls which produce an artifact due to possible adsorption of fluorescein onto PDMS). The images appeared uniform across a 300 μm x 300 μm view field. By averaging the intensity over this constant area, we built the calibration

plot on Fig. 2.(b). The major intensity change occurs between pH 5 and 7, the slow increase between pH 8 and 11 (far above the last pKa of fluorescein) being ascrible to a possible interference with the buffers. These results are in good agreement with cited work.[19, 20] For the CLSM pH-mapping measurements, 6 μM fluoresein sodium solution acidified in hydrochloric acid (pH~0.10) was injected in the inner flow with a volumetric rate flow Q_{in}. For the nanopartciles synthesis experiments, the inner solution was replaced by a mixture of iron salts solution of a total concentration $c = 10^{-2}$ $mol.L^{-1}$ with 0.5 as molar ratio Fe(II)/Fe(III) prepared by mixing $FeCl_3$ and "fresh' $FeCl_2.4H_2O$ salts in diluted and degased hydrochloric acid (pH ~ 0.10). The outer flow in the two experiments was an alkaline solution of tetramethylammonium (TMAOH, 0.172 $mol.L^{-1}$) which was injected with an outer voulumetric rate flow Q_{out}.

2.2 CLSM Measurements

The CLSM measurements were taken on the device shown in Fig. 1 mounted on a three-axis piezostage. This device consisted of two syringe infusion pumps (Harvard apparutus, Picoplus) that provide constant flow using various Becton Dickinson syringes of 1, 3 and 30ml capacity. All componenets were interconnected with PTFE tubing (500 μm i.d.) up to the coaxial microreactor. The coaxial jet microreactor consisted of an outer capillary molded in polydimethylsiloxane (PDMS, Sylgard184) of 1.7mm diameter in which a fused silica capillary (Polymicro Technologies Inc) of 150 μm i.d x 350 μm o.d is fixed through the tip of a micropipette (Gilson). The conical shape of the micropipette enables the inner capillary's position to be easily centred in the outer capillary. The length of the reaction zone from the confluence region to the outlet is almost 3 cm.

To image the pH gradients in the microchannel, 6 μM fluoresein solution in HCl (pH~0.10) and the alkaline solution of TMAOH 0.172 $mol.L^{-1}$ were respectively injected in the inner and the outer flows . The volumetric rate flows Q_{in} and Q_{out} were varied by steps in order to achieve different values of the jet diameter and hence to vary the mixing time, a stationnary flow being always reached after a few seconds of transient regime.

CLSM images of concentration gradients were acquired using a confocal laser scanning microscope (Leica Tandem Scanner SP5 microscope). The confocal setup is based on a DMI6000 inverted microscope with 5 x objective (0.11 NA), used with a pinhole opened to 1 U.A leading to a theoretical Z resolution of 58μm. The fluorescent dye was excited using the 488 nm laser line of Argon laser of sufficiently low power such that photobleaching was negligible, and emited fluorescence was captured between 500 to 600 nm. Typical scans were 3.1mm in X dimension, 0.78 mm in Y dimension and 0.4 mm in Z dimension. The images acquired with a camera of 12 bits sensibility range were converted to 32 bits for image analysis using ImageJ NIH software©.

3 Theory

Modeling of the hydrodynamic and of the mass transport in the microreactor was carried out using a commercial nonlinear solver (FEMLAB by Comsol Inc., version 3.5) to solve iteratively the state equations. Simulations were run on a Mac Pro with 8 GB RAM and 2x3-GHz Quad-Core Intel processors.

Since the microchannel in the concentric microreactor has a cylindrical shape with axial symmetry, we examined the flow in the microchannel in cylindrical coordinates (r,θ,z). Here r is the coordinate in the radial direction of the microchannel, θ the coordinate in circumferential direction, and z the coordinate in the flow direction. Besides, the rotational symmetry of the boundary conditions around the central flow axis enables to derive the numerical solutions in the half-plane of a 2D axisymmetric model. The origin of the coordinates was set at the merging point of the inner and the outer flows located on the axis of symmetry (Fig. 3). Please note that we refer to the plane (z,r) in the simulations as the plane (X,Y) in the CLSM images.
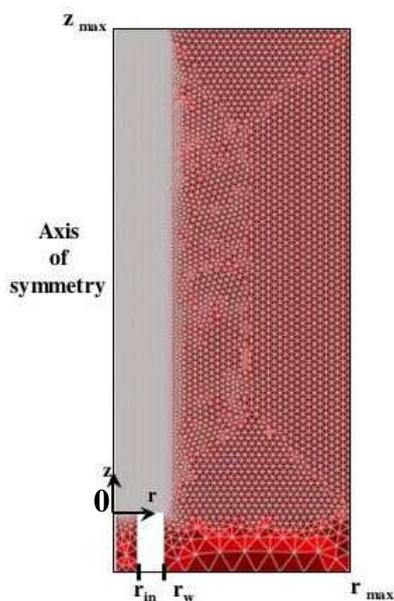

Fig. 3 Meshes used in the modelling of the coaxial flow microreactor. r_{in} is the inner radius of the inner capillary (75 µm), r_w is the outer radius of the inner capillary (175µm) and r_{max} is the radius of the PDMS capillary (0.85 mm). The model is solved with 24000 elements and the density of the mesh is the highest in all the region for $r \leq r_w$.

3.1 The model

The pH distribution in the reactor and the local fluorescein concentration has been predicted by modelling the flow of the various species in the system. The evolution of the concentration $C_i = C_i(\mathbf{r},t)$ of solute particles i follows the continuity equation

$$\frac{\partial C_i}{\partial t} + \mathrm{div}(C_i\mathbf{u} + \mathbf{j}_i) = \sigma_i \tag{1}$$

$\mathbf{u}$ is the hydrodynamic velocity in the channel. It is calculated from the Navier-Stokes equation together with the compressibility condition. For a dilute system, it is identified to the local average velocity of the solvent. $\boldsymbol{\sigma_i}$ is the creation term. It represents the local creation rate of particles due to the chemical reactions. $\mathbf{j}_i$ is the diffusive flux of species i. The general expression of the $\mathbf{j}_i$'s can be obtained from non-equilibrium thermodynamics.[21] For a dilute solution cross correlations are negligible and it reduces to the Nernst-Planck expression[22, 23] :

$$\mathbf{j}_i = -D_i\,\mathbf{grad}\,C_i + \frac{D_i}{k_{\mathrm{B}}T}C_i Z_i e\mathbf{E} \tag{2}$$

With D_i and Z_i respectively the diffusion coefficient and the charge number of species i. e is the elementary charge, k_{B} is Boltzmann's constant and T is the temperature. The local electric field $\mathbf{E}$ depends on the concentrations of the ions $C_i(\mathbf{r},t)$. It can be calculated either from the Henderson approximation, which supposes the local electroneutrality condition, or from the Poisson equation. The time scale of the electrostatic relaxation in the system corresponds to the Debye time, which is equal to a few picoseconds. It is much smaller than the time scale of the experiments. Consequently, at any time the charge distribution has the time to relax and the local electroneutrality condition $\sum Z_i C_i = 0$ is valid. The electric field $\mathbf{E}$ is chosen to satisfy this condition (Henderson field).

The various solute species i are $H^+_{(aq)}$, $OH^-_{(aq)}$, Cl^-, TMA^+ and the fluorescein. Diffusion coefficients were estimated from the value at infinite dilution: D_{H^+} = 9.2 x 10^{-9}, D_{Cl^-} = 2.03 x 10^{-9}, D_{OH^-} = 5.28 x 10^{-9}, D_{TMA^+} = 2 x 10^{-9} $m^2.s^{-1}$.

To simulate the different fluorescein species during the acid-base reaction between HCl and TMAOH we made the following assumptions: (i) fluorescein is diluted in the hydrochloric acid, so no need to account for its charge. Convection diffusion equation with no chemical reaction can be solved to calculate the local concentration map of the total fluorescein denoted Flu; (ii) Fluorescein is diluted compared to H^+ concentration in the acidified fluorescein solution and can not interfer during the acid base-reaction; (iii) The different ionic species of the fluorescein have the same diffusion coefficient $D \approx 0.2$ x 10^{-9} $m^2.s^{-1}$.

After calculating the local pH in the microreactor, the convection diffusion equation was solved for the fluorescein dye. Since the acid-base reactions are virtually instantaneous, it can be assumed that chemical equilibriums are locally achieved for the different fluorescein species.

Since F^{-2} is the only species that can be followed by CLSM, the following reactions were considered:

$$F^0 \Leftrightarrow F^{-1} + H^+ \quad pKa_1 = 4.31 \tag{3}$$

$$F^{-1} \Leftrightarrow F^{-2} + H^+ \quad pKa_2 = 6.27 \tag{4}$$

In each point $(\mathbf{r},z)$, the fluorescein mass balance gives:

$$Flu = F^0 + F^{-1} + F^{-2} \tag{5}$$

By introducing the equilibrium constant Ka_1 and Ka_2 the local concentration of the different species F^{-2} and F^{-1} can be

calculated:

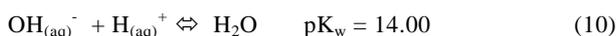$$F^{-2} = \beta \times Flu \qquad (6)$$

$$F^{-1} = \beta' \times F^{-2} \qquad (7)$$

With

$$\beta = 1 + \frac{H^+}{K_{a_1} \times K_{a_2}} + \frac{H^+}{K_{a_2}} \qquad (8)$$

$$\beta = \frac{H^+}{K_{a_2}} \qquad (9)$$

The term of chemical kinetics is not zero for $H^+_{(aq)}$, $OH^-_{(aq)}$ because of the dissociation equilibrium:

$$OH^-_{(aq)} + H^+_{(aq)} \Leftrightarrow H_2O \qquad pK_w = 14.00 \qquad (10)$$

For a dilute solution, in the most general case, the resulting σ_i term for $H^+_{(aq)}$ and $OH^-_{(aq)}$ is:

$$\sigma_{H^+} = \sigma_{OH^-} = \sigma = f(\{C_i\})(C_{H^+}C_{OH^-} - K_w) \qquad (11)$$

where K_w is the water dissociation constant. The term $f(\{C_i\})$ expresses the kinetics of the reaction. In principle, the evolution of the concentration depends on $f(\{C_i\})$. However, in our case, the dissociation kinetics is very fast. In particular, it is much faster than the time scale of the experimental measurements in the reactor. Accordingly the resulting evolution of the concentration should not depend on the exact expression of $f(\{C_i\})$. This can be shown by eliminating the fast variables,[24] as it is explained in the appendix. Thus it is practically possible to describe the system by assuming that $f(\{C_i\})$ is constant:

$$\sigma = k(C_{H^+}C_{OH^-} - K_w) \qquad (12)$$

If k is chosen to be large enough, the evolution of the concentration does not depend on its value because the system is in the regime where chemical kinetics is a fast variable.

3.2 Validation

The model has been solved numerically for the geometry represented in Fig. 3, for different flow rates of the inner and the outer tubes Q_{in} and Q_{out}. In the inner solution, the concentrations of the various species were 0.794 mol.L^{-1} for H^+ and Cl$^-$. In the outer solution, they were 0.172 mol.L^{-1} for OH^- and TMA$^+$.
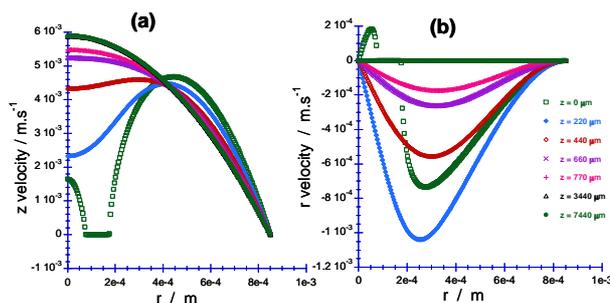
Fig. 4 (a) z velocity; (b) r velocity at different positions from the point of confluence in the microreactor showing the hydrodynamic transition till a laminar Poiseuille profile is established.

The longitudinal and radial components of the hydrodynamic velocity field are represented in Fig. 4. The two injected Poiseuille flows diffuse and mix so that they rapidly become a unique Poiseuille flow. The hydrodynamic transient time is roughly related to the kinematic viscosity of water ν and to the size of the capillary R by R^2/ν. The corresponding entrance length for an average fluid velocity U is $UR^2/\nu = R \times \mathrm{Re}$ .where Re stands for the Reynold number which is small in the laminar regime. The radius of the inner stream after the transient hydrodynamic regime follows the flow conservation law:

$$R_s^2 = R^2 \left[1 - \left(\frac{1}{1/\alpha + 1} \right)^{1/2} \right] \qquad (13)$$

Where R_s denotes the inner stream radius when the Poiseuille flow is developped, R the radius of the PDMS capillary and α the volumetric rate ratio ($\alpha = Q_{out}/Q_{in}$).
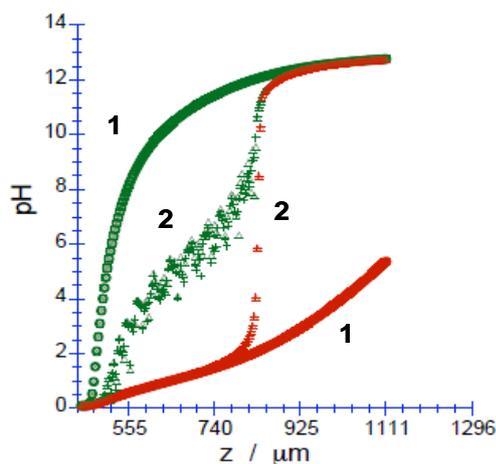
Fig. 5 pH curves obtained from $pH_{H^+} = -\log[H^+]$ (red curves) and from $pH_{OH^-} = 14 + \log[OH^-]$ (green curves) when k is increased from 1 to 10^7 L/(mol.s^{-1}) (curves 1) and for k = 10^8 and 10^9 L/(mol.s^{-1}) (curves 2) for a volumetric rate flow ratio α = 400 and Z_{max} = 1100 μm

An important issue is the choice of the parameter k. Fig. 5 shows a parametric study of the theoretical pH obtained along the axis of symmetry in the microreactor when the value of k

18100 | *J. Phys. Chem.* C 2009, *113*, No. 42

Abou-Hassan et al, authormanuscript

is increased from 1 to 10^9 L/(mol.s^{-1}). The pH values were calculated from the local H$^+$ concentration [H$^+$] with $pH_{H^+} = -\log[H^+]$ and the local OH$^-$ concentration [OH$^-$] with $pH_{OH^-} = 14 + \log[OH^-]$. For small values of k, from 1 to 10^7 L/(mol.s^{-1}) pH_{H^+} is different from pH_{OH^-}, the chemical equilibrium does not have the time to be established, and the two ions diffuse independantly. If k is increased (k $\geq 10^8$ L/(mol.s^{-1})), all the pH_{H^+} curves merge together and become similar to a titration curve between TMAOH and HCl. Similarly for the same values of k (k $\geq 10^8$ L/(mol.s^{-1})), the pH_{OH^-} follows the same titration curve, for most of the z values which indicates that the chemical equilibrium is reached. Actually, there is in the intermediate acid domain for which the pH_{OH^-} curve is greater than the pH_{H^+}. If k is increased, this part of the pH_{OH^-} curve does not gather on the pH_{H^+} titration curve but becomes more and more noisy. By refining the mesh in that domain it should be possible to obtain the same titration curve as pH_{H^+} in the whole concentration range but this requirement overcomes the possibilities of the computer memory. In fact, this noisy domain corresponds to the domain for which OH$^-$ concentration is negligible compared to the other concentrations and the pH is driven by the H$^+$ concentration. Accordingly, all the simulations were run with k = 10^9 L/(mol.s^{-1}) and the pH has been estimated from the H$^+$ concentration.

4. Results and Discussion

A series of volumetric ratio values chosen between 400 and 40 was applied, a delay of a few seconds being respected each time before capturing the CLSM images in order to enable the new stationnary flow and concentration profiles to establish in the microreactor. Fig. 6 shows the steady-state 2D fluorescence profile obtained by confocal slicing in the middle of the outlet of the inner capillary where acidified fluorescein solution (6 μM) flows in the centre surrounded by the outer alkaline TMAOH solution upon application of a volumetric ratio α = 400. Since the microreactor is cylindrical, a 3D image can be obtained by rotation of that plane around the axis of symmetry. After "Z-stacking" of the 20 X-Y slices, CLSM cross sections in the X-Z plan at different positions from the tip of the inner capillary show a disk shape fluorescence that mirrors the diffusion profile and the establishement of pH gradients in the central jet. The fluorescence burst in the central jet is due to the deprotonation of fluorescein by the hydroxide ions diffusing towards the center that remain in excess after reaction with H$^+$. The hollow cylindrical shape on the fluorecence image (cross-sections (1) and (2) of the central stream) illustrates the transition from a still acidic core (below pH 4) of the stream to a neutralized "skin" near the pKa of 6.2 of fluorescein. It is exactly in this boundary region near the pH equivalence that we expect the coprecipiration of the iron salts in a synthesis experiment with the same hydrodynamic ratio. However, we cannot deduce a pH mapping by inverting directly the images such as Fig. 6 using the calibration cuve intensity *vs.* pH of Fig. 2(b). From a mathematical point of view, this curve should be sigmoidal, which means that no difference in the fluorescence intensity should exist for pH higher than 7 or

repectively lower than 4. This is not verified experimentally, as we see that the curve does not reach perfectly a plateau. Besides, fluorescein diffusion from the inner stream to the outer stream occurs so that pH values deduced from the calibration curve can be underestimated. Please note that we could not perfuse fluoresceine both in the outer and the inner flows as in the calibration experiment, because the inner jet would have appeared as a dark cylinder inside a bright (because alkaline) surrounding stream, so that their interface would have been very difficult to distinguish by CLSM. To avoid all these experimental issues, and in order to reach the true mapping of pH gradients in the micoreactor, we have calculated the spatial distribution of F^{-2} and pH numerically. Then by comparison to the experimental intensity cross-sections, we can deduce the corresponding distribution of pH gradients.
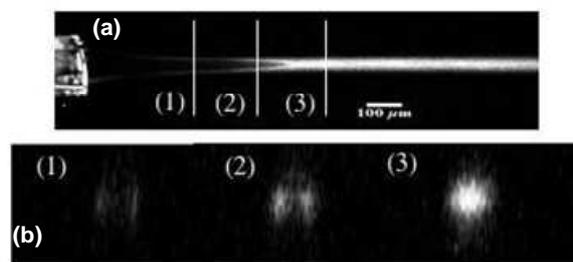

Fig.6 (a) CLSM image of the acid-base reaction in presence of 6 μM fluorescein solution in the inner flow with an applied volumetric rate flow α = 400. The image was recorded in the X-Y plane. (b) The three images are X-Z images, taken at the locations indicated by (1), (2) and (3), constructed from a "Z-stack". The Z-stack consisted in 20 slices, which were spaced at 20 μm intervals.

After background substraction, the measured fluorescence intensity is directly proportional to the F^{-2} concentration with a constant of proportionality that we calculated by the following method: at first, we extracted the experimental curves I(r) from different cross-sections at constant z deduced from the stack of images; then we compared them to the numerical simulations of the F^{-2} concentration field. The experimental fluorescence curves were fitted and the best fit were obtained with $I_{exp} = 2.56 \times 10^{+5} \times F^{-2} + 6.39$, where 6.39 value accounts for the background.
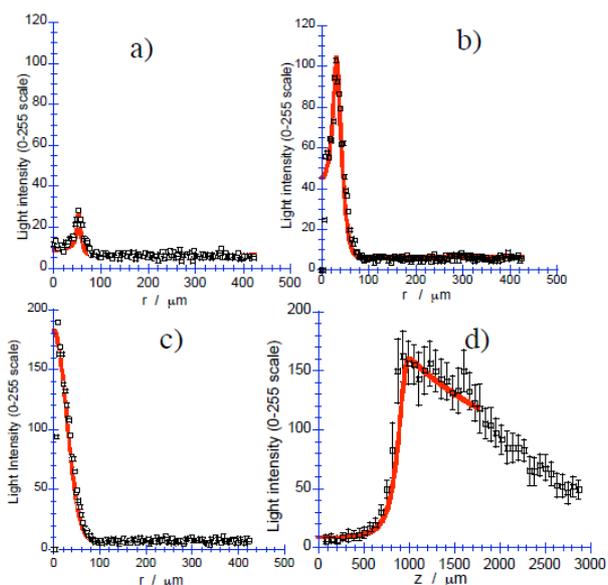
Abou-Hassan et al, author manuscript

J. Chem. Phys. C 2009 *113*, No. 42 | **18101**

Fig.7 Radial (a, b, c) and longitudinal at r = 0 (d) cross sections of the fluorescence intensity as measured experimentally (□) and calculated numerically (lines) for different positions z = 440; 770 and 1575 μm from the point of confluence.

Fig. 7 shows the experimental and predicted fluorescence intensities profiles for α = 400 at different positions in the channel and the good agreement between the theoretical and experimental curves. Besides, the left part of the longitudinal cross-section of Fig 7.d (for z ≤ zc ≈ 1000 μm) can be fitted by a sigmoidal shape, which is coherent with a regular increase of pH according to the calibration curve of Fig 2.b. The right part of the curve (for z ≥ z_c ≈ 1000 μm) exhibits a linear decrease of the intensity with increasing z. This observation evidences two regimes : (i) for z ≤ z_c ≈ 1000 μm the concentration field is controlled by both the reaction and diffusive processes, so that a sigmoidal intensity curve is observed ; (ii) for z ≥ z_c, the system evolves only through a diffusive process, by which the fluorescein molecules diffuse radially thus decreasing the fluorescence intensity locally around the r = 0 axis. The variation in the fluorescence intensity in the first regime is then related to the pH and to the local variations in concentration due to diffusion, while in the second regime, the fluoresence intensity is related to the variation in the local concontration field of the fluorescent dye. To illustrate the good agreement between the CLSM experiment and the model, Fig. 8 compares the 2D fluorescence intensity map of fluorescein represented by a scale from cold (low intensity) to warm colors (high levels). The symmetry between the experimental part of the image on the left and the calculated one on the right is a clear evidence that the assumptions made to calculate the diffusion of the fluorescein species and the acid-base reaction (paragraph 3.1) are acceptable.
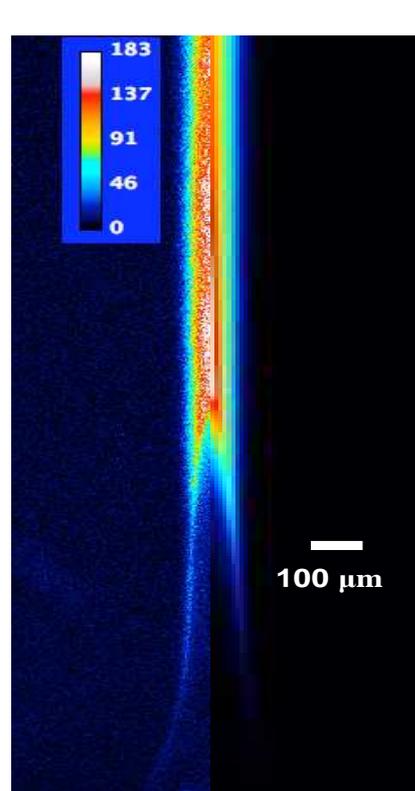

Fig. 8 Comparison of the experimental and predicted fluorescence intensities in the X-Y plane with (a) the left half-plane representing the experimental fluorescence intensity and (b) the right half-plane with the predicted fluorescence intensity for α = 400.

In addition, the CLSM image can be compared to the simulated pH in the microreactor. Fig. 9 shows this comparaison in the 2D model. As the acidic fluorescein solution flows in the centre, OH^- ions diffuse from the outer stream to the inner stream elevating the pH and the local concentration of F^{-2} which is reflected by increasing the fluorescence. pH gradients are established in the inner stream in the radial and the longitudinal directions. The dye fluorescence intensity follows exactly the pH gradients in the two dimensions. For example, the boundary between dark and bright levels on the left image is perfectly symmetrical to the pH equivalence in yellow and green (pH 6-7) on the right one.
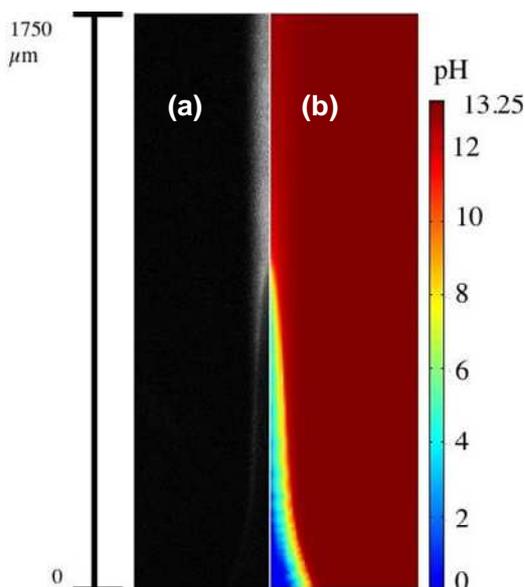
Abou-Hassan et al, author manuscript

Fig. 9 Comparison in the X-Y plane between (a) CLSM image of the fluorescein and (b) the theoretical pH profiles in the central stream for α =400.

Finally, the flow rates ratio α was tuned between 40 and 400 and the corresponding fluorescence profiles along the r = 0 axis were compared on Fig. 10.a. The good matching between the predicted and the experimental intensity curves for several values of α clearly validates our method.
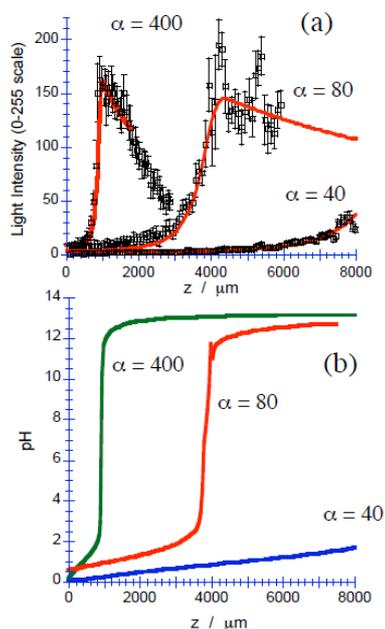

Fig. 10 (a) Evolution of the experimental fluorescence profiles (□) when α = 40; 80 and 400 along the symmetry axis (r = 0). The lines represent the predicted fluorescence intensities calculated for each case from the simulated F^{-2} concentrations, (b) Simulated pH profiles along the symmetry axis (r = 0) for α = 40; 80 and 400

As fluorescein is just a pH reporter dye, these curves can be interpreted from the results of the pH calculations (Fig. 10.b). As expected, the shape of the pH curves are typically of a titration by a stong base (TMAOH) of a strong acid (HCl). When α increases, the squeezing effect of the inner stream by the outer stream increases; the inner stream containing the fluorescein dye and HCl is focalised (eq. 13), thus OH^- diffusion pathways to the H^+ ions are reduced. This decrease of the diffusion distance between the reagent species implies a faster mixing and a steeper jump of pH near the equivalence point (pH = 7).

To understand how these results can affect the synthesis of the superparamagnetic nanoparticles, we have to remind the difficulties in synthesizing iron oxide nanoparticles by bulk coprecipitation, including the control of their particles size, size distribution, and especially the resultant phase. Many possible non magnetic phases, such as ferrihydrite, akaganeite (β-FeOOH), Fe(OH)3, etc, may be produced at different reaction conditions. To get pure magnetite nanoparticles Fe_3O_4 $(Fe^{II}Fe_2^{III}O_4)$ which is the phase of the superparamagnetic nanoparticles, other than an appropriate mole ratio of Fe^{2+} to Fe^{3+} a fast pH range must be fulfilled to get anticipant phase in the coprecipitation reaction. Jolivet et al.[25] proposed that electron transfer between Fe^{2+} and Fe^{3+} plays a pivotal role in the formation of the magnetic nanoparticles, and it is the absorption of Fe^{2+} that makes quasi amorphous ferric hydroxide transform into spinel magnetite. Kim et.al.[26] also suggested that in the pH range of 1–4, Fe^{3+} condenses as FeOOH, and that Fe_3O_4 is obtained only in the pH range of 9–14. Thus a fast alkaline jump is required to prevent the formation of FeOOH phase intermediate.

In view of these results and in order to synthesize magnetic nanoparticles, α = 400 seems to be the best suitable case, because it offers the advantage of fast mixing and fast pH jump . The choices α = 80 and 40 would lead to an expected decrease of the yield of magnetic nanoparticles due to the precipitation of antiferromagnetic iron hydroxides. These results have been used to produce the stable and colloidal magnetic nanoparticles described in details in our previous work[8]. Fig. 12 shows the Transmission Electron Microscopy of the synthesized magnetic nanopartciles for α = 400.
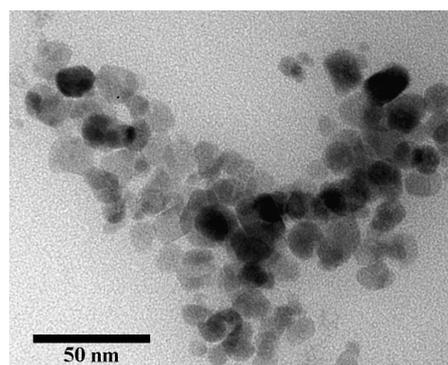

Fig. 12 TEM image of magnetite nanoparticles prepared by coprecipitation of iron(II) and iron(III) salts by addition of TMAOH for α = 400

5 Conclusions

Through a series of investigations comparing CLSM images

with numerical simulations, we have demonstrated the quantitative three dimensional mapping of the pH indicator concentration in the inner and outer streams of a coxial flows microreactor. The experimental fluorescence images
[5] superpose well to the numerical simulations of concentrations obtained by solving the underlying mass transport equations of the different species, taking into account the acid-base reaction inside the focalized flow. This simple model proposed to solve the fluorescein distribution in the
[10] microreactor during the chemical reaction proved to be accurate enough to deduce the precise localization of pH gradients inside the channel and to choose the right hydrodynamic parameters needed for the elaboration of superparamagnetic iron oxide nanoparticles. A step further in
[15] the chemical engineering model will be to consider the coprecipitation reaction itself including the precursor salts and the colloidal products, in order to evidence a possible improve of the size monodispersity due to the confinement of the reaction at the interface between the coaxial flows.
[20]

Acknowledgments

Appendix

The fact that the chemical kinetics is fast can be modelled by replacing $f(\{C_i\})$ by $g(\{C_i\})/\varepsilon$ with ε a small parameter. We
[30] shall derive the evolution of the system in the limit $\varepsilon \to 0$.

Let i a solute particle different from $H^+_{(aq)}$ and $OH^-_{(aq)}$, and j either $H^+_{(aq)}$ or $OH^-_{(aq)}$. The evolution of the concentration follows the equations

$$\frac{\partial C_i}{\partial t} = -\mathrm{div}(C_i\mathbf{u}) + D_i\Delta C_i + \mathrm{div}\left(\frac{D_i}{k_B T}C_i Z_i e\mathbf{E}\right)$$

[35]
$$\frac{\partial C_j}{\partial t} = -\mathrm{div}(C_i\mathbf{u}) + D_j\Delta C_j + \mathrm{div}\left(\frac{D_j}{k_B T}C_j Z_j e\mathbf{E}\right) + \frac{g(\{C_i\})}{\varepsilon}(C_{H^+}C_{OH^-} - K_w)$$

To emphasize that we are interested in the behaviour of the slow variables and want to eliminate the fast variables, we adjust the time by setting $t = \varepsilon\tau$:

[40]
$$\frac{\partial C_i}{\partial \tau} = -\varepsilon\,\mathrm{div}(C_i\mathbf{u}) + \varepsilon D_i\Delta C_i + \varepsilon\,\mathrm{div}\left(\frac{D_i}{k_B T}C_i Z_i e\mathbf{E}\right)$$

$$\frac{\partial C_j}{\partial \tau} = -\varepsilon\,\mathrm{div}(C_j\mathbf{u}) + \varepsilon D_j\Delta C_j + \varepsilon\,\mathrm{div}\left(\frac{D_j}{k_B T}C_j Z_j e\mathbf{E}\right) + g(\{C_i\})(C_{H^+}C_{OH^-} - K_w)$$

It is clear that for small ε the variables C_i vary in a slower time than C_j. τ corresponds to the fast time scale and t is the slow one. Actually $C_d = C_{H^+} - C_{OH^-}$ is also a slow variable as it can be
[45] understood by writing the evolution of the concentration of $H^+_{(aq)}$ and $OH^-_{(aq)}$ in terms of C_d and $C_s = C_{H^+} + C_{OH^-}$.

$$\frac{\partial C_s}{\partial \tau} = \varepsilon Y_s + \frac{g(\{C_i\})}{2}\left((C_s + C_d)(C_s - C_d) - 4K_w\right)$$

$$\frac{\partial C_d}{\partial \tau} = \varepsilon Y_d$$

Y_s and Y_d are two terms, which depend on $\mathbf{u}$ and on the
[50] various local concentrations. They are directly obtained from the preceding equations. Consequently C_s is the only fast variable since it is the only one that does not become constant for $\varepsilon \to 0$. Let's substitute for C_s a power series in ε

$$C_s = C_s^0 + \varepsilon C_s^1 + \mathsf{K}$$

[55] and let's require that the various orders of ε vanish separately when the evolution equations are written in the slow time scale:

$$\frac{\partial C_s}{\partial t} = Y_s + \frac{g(\{C_i\})}{2\varepsilon}\left((C_s + C_d)(C_s - C_d) - 4K_w\right)$$

$$\frac{\partial C_d}{\partial t} = Y_d$$

[60] The term of order ε^{-1} reads

$$0 = \frac{g(\{C_i\})}{2}\left((C_s^0 + C_d)(C_s^0 - C_d) - 4K_w\right)$$

This equation corresponds to the local chemical equilibrium

$$(C_s^0 + C_d)(C_s^0 - C_d) = 4K_w$$

[65]

It determines C_s^0 as a function of C_d. Substitution of $C_s = C_s^0(C_d)$ in the equation of evolution for C_d and the C_is gives the evolution of the slow variables. At that level of approximation, the fast variable C_s follows instantaneously
[70] the slow variable in order to satisfy the chemical equilibrium. Furthermore, the evolution of the slow variables does not depend on the kinetic term $g(\{C_i\})/\varepsilon$.

[75] ## Notes and references

[a] *Laboratoire Physicochimie des Electrolytes Colloïdes et Sciences Analytiques (PECSA), UMR 7195 CNRS / UPMC / ESPCI, Université Pierre et Marie Curie (Paris 6), 4 place Jussieu, case 51, 75252 Paris CEDEX 5, France. Fax: +33 (1) 44273228; Tel: +33 (1) 44273169;*
[80] *E-mail: ali.abou_hassan@upmc.fr*
E-mail: jean-francois.dufreche@upmc.fr

1. S. Sun, C. B. Murray, D. Weller, L. Folks and A. Moser, *Science*,
[85] 2000, **287**, 1989-1992.
2. J. P. Fortin, C. Wilhelm, J. Servais, C. Menager, J. C. Bacri and F. Gazeau, *J. Am. Chem. Soc.*, 2007, **129**, 2628-2635.
3. M. M. Miller, G. A. Prinz, S. F. Cheng and S. Bounnak, *Appl. Phys. Lett.*, 2002, **81**, 2211-2213.
[90] 4. I. Chourpa, L. Douziech-Eyrolles, L. Ngaboni-Okassa, J. F. Fouquenet, S. Cohen-Jonathan, M. Soucé, H. Marchais and P. Dubois, *Analyst*, 2005, **130**, 1395-1403.
5. M. S. Martina, J. P. Fortin, C. Menager, O. Clement, G. Barratt, C. Grabielle-Madelmont, F. Gazeau, V. Cabuil and S. Lesieur, *J. Am.*
[95] *Chem. Soc.*, 2005, **127**, 10676-10685.
6. A. J. deMello and J. C. deMello, *Lab. Chip*, 2004, **4**, 11N.

7. Y. Song, J. Hormes and C. S. S. R. Kumar, *Small*, 2008, **4**, 698-711.
8. A. Abou Hassan, O. Sandre, V. Cabuil and P. Tabeling, *Chem. Commun.*, 2008, 1783-1785.
9. A. Abou-Hassan, O. Sandre, S. Neveu and V. Cabuil, *Angew. Chem. Int. Ed.*, 2009, **9999**, NA.
10. K. Jähnisch, V. Hessel, H. Löwe and M. Baerns, *Angew. Chem. Int. Ed.*, 2004, **43**, 406-446.
11. W. Ehrfeld, V. Hessel and H. Lowe, *Microreactors: New Technology for Modern Chemistry*, Wiley VCH, Weinheim, 2000.
12. B. F. Cottam, S. Krishnadasan, A. J. DeMello, J. C. DeMello and M. S. P. Shaffer, *Lab. Chip*, 2007, **7**, 167-169.
13. J. Pawliszyn, *Anal. Chem.*, 1992, **64**, 1552-1555.
14. T. Ozeki and D. E. Irish, *J. Electroanal. Chem.*, 1990, **280**, 451-455.
15. C. Amatore, F. Bonhomme, J.-L. Bruneel, L. Servant and L. Thouin, *Electrochem. Commun.*, 2000, **2**, 235-239.
16. R. O'Malley, A. Vollmer, J. R. I. Lee, I. Harvey, J. Headspith, S. Diaz-Moreno and T. Rayment, *Electrochem. Comm.*, 2003, **5**, 1-5.
17. C. J. Slevin and P. R. Unwin, *Langmuir*, 1997, **13**, 4799-4803.
18. C. J. R. Sheppard, D. M. Hotton and D. Shotton, *Confocal Laser Scanning Microscopy (Microscopy Handbooks)*, BIOS Scientific Publishers, 1997.
19. D. Margulies, G. Melman and A. Shanzer, *Nat. Mater.*, 2005, **4**, 768-771.
20. S. Fiedler, R. Hagedorn, T. Schnelle, E. Richter, B. Wagner and G. Fuhr, *Anal. Chem.* 1995, **67**, 820-828.
21. S. R. de-Groot and P. Mazur, *Non-Equilibrium Thermodynamics*, Dover, 1983.
22. P. Turq, J. Barthel and M. Chemla, *Transport, Relaxation and Kinetic Processes in Electrolyte Solutions*, Springer-Verlag, 1992.
23. B. J. Berne and R. Pecora, *Dynamic Light Scattering*, Dover, 2000.
24. N. G. Van Kampen, *Phys. Rep.*, 1985, **124**, 69.
25. E. Tronc, P. Belleville, J.P. Jolivet, J. Livage, *Langmuir*, 1992, **8**, 313-319
26. D.K. Kim, M. Mikhaylova, Y. Zhang, M. Muhammed, *Chem. Mater.* 2003, **15**, 1617-1627

1.   Mathematical demonstration of equation 13

The equation of the inner stream radius can be derived as follow from the flow conservation of incompressible fluids.
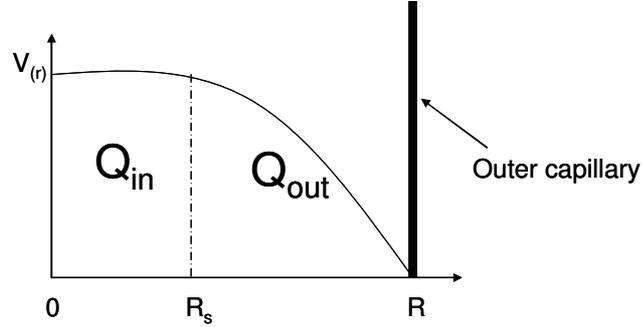

Figure 1. Schematic representation of the Poiseuille flow developed in the channel. R_s is the inner stream radius. R is the PDMS radius (0.85 mm). Q_{in} is the inner stream rate flow and Q_{out} is the outer stream rate flow.

After the entrance length the Poiseuille flow is fully developed:

$$v_{(r)} = v_0\left(1-\left(\frac{r}{R}\right)^2\right) \tag{1}$$

$$Q_{tot} = \int_0^R v(r)dr = \frac{\pi}{2}v_0 R^2 \Rightarrow v_0 = \frac{2Q_{tot}}{\pi R^2} \tag{2}$$

$$Q_{in} = \int_0^{R_s} v(r)dr = v_0 \pi R_s^2 - \frac{\pi v_0}{2}\frac{R_s^4}{R^2} \tag{3}$$

Substituting $v_0 = \dfrac{2Q_{tot}}{\pi R^2}$ in the equation (3) then by arranging it after dividing by Q_{tot} we obtain

the second order equation (4) with $\left(\dfrac{R_s}{R}\right)^2$ being the variable x.

$$x^2 - 2x + \frac{Q_{in}}{Q_{tot}} = 0 \tag{4}$$

$$\boxed{R_s^2 = R_c^2\left(1-\left(\frac{1}{1/\alpha+1}\right)^{1/2}\right)} \tag{5}$$
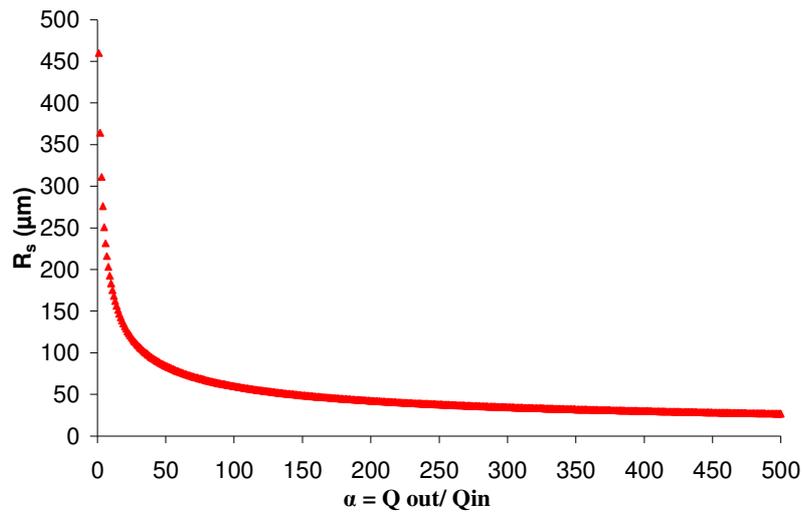
with $\alpha = \dfrac{Q_{out}}{Q_{in}}$.

Figure 2. This curve shows the variation of the inner jet stream when α is varied. Three domains are observed on this curve: 1/ for $0 \leq \alpha \leq 50$; 2/ for $50 \leq \alpha \leq 200$ and 3/ $\alpha > 200$. We studied 3 cases in our simulations, from each domain: $\alpha = 40$; 80 and 400.